# On the detectability of Galactic dark matter annihilation into monochromatic gamma-rays*

TANG Zhi-Cheng(唐志成)[1)] YUAN Qiang(袁强)
BI Xiao-Jun(毕效军) CHEN Guo-Ming(陈国明)

Institute of High Energy Physics, Chinese Academy of Sciences, Beijing 100049, China

**Abstract:** Monochromatic $\gamma$-rays are thought to be the smoking gun signal for identifying dark matter annihilation. However, the flux of monochromatic $\gamma$-rays is usually suppressed by virtual quantum effects since dark matter should be neutral and does not couple with $\gamma$-rays directly. In this work, we study the detection strategy of the monochromatic $\gamma$-rays in a future space-based detector. The flux of monochromatic $\gamma$-rays between 50 GeV and several TeV is calculated by assuming the supersymmetric neutralino as a typical dark matter candidate. The detection both by focusing on the Galactic center and in a scan mode that detects $\gamma$-rays from the whole Galactic halo are compared. The detector performance for the purpose of monochromatic $\gamma$-ray detection, with different energy and angular resolution, field of view, and background rejection efficiencies, is carefully studied with both analytical and fast Monte-Carlo methods.

**Key words:** dark matter, line emission, gamma-ray, detectability

**PACS:** 95.35.+d, 98.35.-a, 98.35.Gi **DOI:** 10.1088/1674-1137/35/8/006

## 1 Introduction

The existence of dark matter (DM) in the universe is widely accepted nowadays. The evidence comes from many astronomical observations, which have observed the gravitational effects of dark matter in different spatial scales, from dwarf galaxies, galaxies and galaxy clusters to the cosmological scale. It is recognized that DM particles should be neutral, cold and non-baryonic, which can only exist in theories beyond the standard model of particle physics. Among the large amount of DM candidates proposed in the literature, the weakly interacting massive particles (WIMP) are the most favored ones, which can account for the observed DM density naturally.

In order to determine the nature of the WIMP DM particles, we generally have three ways to probe the interaction between the DM particles and the standard particles: direct detection measures the scattering by DM with the detector nuclei; or measurement of DM particles directly produced in a powerful collider, such as LHC or ILC; finally indirect detection searches for DM annihilation or decay products in cosmic rays (CRs), including gamma-rays, electrons, positrons, protons, antiprotons and neutrinos. For indirect detection, the gamma-rays are usually the best probe of DM because they are not deflected by the magnetic field during the propagation. Further, the technology of the high energy gamma ray detector has developed very fast in recent years. In general, gamma-rays are produced through the hadronization and decay of the DM annihilation/decay final states, and they have continuous energy spectra. Another annihilation channel is the monochromatic gamma-rays with a small branching ratio via a loop diagram. Since there are large diffuse backgrounds of gamma-rays, it is usually not easy to figure out the continous DM signals from the background. On the other hand, although the monochromatic gamma rays have a smaller cross section and lower flux, they are not going to mix with other astrophysical processes. Therefore, the mono-

Received 5 November 2010, Revised 14 January 2011

* Supported by Natural Science Foundation of China (10435070, 10773011, 10721140381, 10099630) and China Ministry of Science and Technology (2007CB16101, 2010CB833000)

1) E-mail: tangzhch@ihep.ac.cn

chromatic gamma-rays by DM annihilation are usually taken as the smoking-gun of the DM signal. If the detector has very good energy resolution, the background will be suppressed and the detectability will be improved.

In this work, we discuss the DM annihilation into monochromatic photons, $\chi_0\chi_0 \to \gamma\gamma$ and $\chi_0\chi_0 \to \gamma Z_0$, with the energy of the gamma-ray photon $m_\chi$ and $(m_\chi - m_Z^2)/4m_\chi$, respectively. Here we neglect the kinetic energy of DM particles since its movement is non-relativistic today. For very massive DM $m_\chi \gg m_Z$, the photon energies of the two channels are identical and cannot be distinguished in experiments. This work tries to give the perspective of detecting such line spectrum gamma-rays from DM annihilation in the Milky Way, and it shows the requirements for detector design.

The $\gamma$-ray flux from DM annihilation is proportional to the annihilation cross section and DM density square. As a typical WIMP DM, we consider the lightest neutralino in the minimal supersymmetric standard model (MSSM) as an explicit example in our calculation. The cross section can be computed given the MSSM model parameters. In this work, we will employ the DarkSUSY package [1] to scan the MSSM parameter space. As for the galactic DM density profile, numerical simulations indicate that DM is highly concentrated in the halo center. Therefore the Galactic center (GC) is usually the first choice in searching for DM signals. In addition, there are also a large number of substructures existing in the halo, mostly in the outer part. The contribution from substructures will also be discussed. The backgrounds for monochromatic photon detection include CR nuclei (mainly protons and Helium for energies $\lesssim 10$ TeV), electrons, diffuse continuous $\gamma$-rays and the $\gamma$-ray point sources in the GC region. The nuclei and electrons can be rejected through the particle identification technique of the detector. For the diffuse $\gamma$-ray background, we need a high energy resolution to suppress the background.

This paper is organized as follows. The MSSM model and the Galactic DM density distribution will be presented in Sec. 2. In Sec. 3, the possible backgrounds in our study are introduced, especially those in the GC region. Sec. 4 gives the results of detection sensitivity for the GC region through a simple analytical estimate. We show in Sec. 5 the sensitivity for all-sky observation in the scan mode, with substructures included, using Monte-Carlo simulation. Finally, we draw the conclusion and discussion in Sec. 6.

## 2 Dark matter annihilation into monochromatic gamma-rays

The $\gamma$-ray flux from DM annihilation can be written as

$$\phi(\psi) = \frac{\rho_\odot^2 R_\odot}{4\pi} \times \frac{N\langle\sigma v\rangle}{2m_\chi^2} \times J(\psi), \tag{1}$$

where $\psi$ is a specified direction away from the Galactic center, $\rho_\odot \approx 0.4$ GeV·cm$^{-3}$ [2, 3] is the local DM density, $R_\odot \approx 8.5$ kpc is the distance from the Sun to the GC, $m_\chi$ is the mass of the DM particle, $\langle\sigma v\rangle$ is the velocity weighted thermal average annihilation cross section, the multiplicity $N = 1, 2$ for $\gamma Z_0$ and $\gamma\gamma$ channels, respectively. Finally, $J(\psi)$ is the line-of-sight integral of the density square

$$J(\psi) = \frac{1}{\rho_\odot^2 R_\odot} \int \rho^2(l) \mathrm{d}l.$$

The $\gamma$-ray flux depends on both the particle parameters and the density distribution of DM.

### 2.1 MSSM dark matter model

Without loss of generality, we take the neutralino in MSSM as a typical WIMP DM in this work. In order to reduce the number of free parameters in MSSM, we only take a few relevant free parameters in our discussion, as done in Ref. [1], that is,

$$\mu,\ M_2,\ M_1,\ \tan\beta,\ M_\mathrm{A},\ m_0,\ A_\mathrm{b},\ A_\mathrm{t}, \tag{2}$$

where $\mu$ is the Higgsino mass parameter, $M_2$ and $M_1$ are the wino and bino mass parameters, respectively, $\tan\beta$ is the ratio of the vacuum expectations of the two Higgs fields, $M_\mathrm{A}$ is the mass of pseudo-scalar Higgs boson, $m_0$ is the universal sfermion mass, $A_\mathrm{b}$ and $A_\mathrm{t}$ are the trilinear soft breaking parameters and the corresponding parameters for the first two generations are assumed to be zero.

We employ DarkSUSY to explore the parameter space of the phenomenological MSSM model [1]. The scan ranges of these parameters are: 50 GeV $< |\mu|, M_2, M_1, M_\mathrm{A}, m_0 <$ 10 TeV, $1.1 < \tan\beta < 55$, $\mathrm{sign}(\mu) = \pm 1$, $-3m_0 < A_\mathrm{t}, A_\mathrm{b} < 3m_0$. There are also other constraints from the theoretical consistency requirements and the accelerator data. Finally, we require the relic density of DM to be $\Omega_\chi h^2 < 0.128$ according to the $3\sigma$ upper limits of WMAP seven years results [4].

### 2.2 Density distribution

The most precise knowledge of the density profile of DM inside the halo comes from numerical simula-

tions. Navarro et al. (1997) found that the density profile is universal for halos of different scales, referred to as the Navarro-Frenk-White (NFW) profile [5]

$$\rho(r)=\frac{\rho_{\rm s}}{(r/r_{\rm s})\,(1+r/r_{\rm s})^2}, \tag{3}$$

where $\rho_{\rm s}$ and $r_{\rm s}$ are two scale parameters depending on the mass and concentration of the halo. However, due to the limit of resolution, some other density profiles with different central behaviors were also proposed in the literature. For example, Moore et al. (1999) proposed a density profile with a much steeper inner slope [6]

$$\rho(r)=\frac{\rho_{\rm s}}{(r/r_{\rm s})^{1.5}\left[1+(r/r_{\rm s})^{1.5}\right]}. \tag{4}$$

Recent simulations have tended to favor the Einasto profile with a gradual flattening of the logarithm slope of the inner behavior [7]. There are also studies showing that the density profile might be non-universal [8]. Considering the diversity of the inner profile of DM density distribution, we adopt NFW and Moore profiles for this study. The model parameters are $r_{\rm s}=20$ kpc, $\rho_{\rm s}=0.35$ GeV·cm$^{-3}$ for the NFW, and $r_{\rm s}=28$ kpc, $\rho_{\rm s}=0.078$ GeV·cm$^{-3}$ for the Moore profile, respectively. The local density for these parameter sets is 0.4 GeV·cm$^{-3}$.

To avoid the divergence of density when $r\to 0$, a cutoff scale is applied considering the fact that there should be a balance between the gravitational infall and the annihilation [9]. For common parameters of DM particles, the maximum density is estimated to be $\sim 10^{18} M_\odot$ kpc$^{-3}$ [10].

### 2.3 Substructures

The cosmological structures form hierarchically in the cold dark matter scenario, that is, the DM collapses to form small halos first, then grows to larger and larger halos through accretion and merger. Numerical simulations show that there are a large number of subhalos surviving the merger history and existing in the Milky Way dark matter halo [11–14]. The dwarf galaxies are part of the Galactic subhalos that have been observed.

According to the simulations, the number density distribution of subhalos as a function of its mass and location can be parameterized as [15, 16]

$$\frac{{\rm d}n}{{\rm d}m_{\rm sub}\cdot 4\pi r^2{\rm d}r}=\frac{n_0}{1+(r/r_{\rm h})^2}\times\left(\frac{m_{\rm sub}}{m_{\rm host}}\right)^{-\alpha}, \tag{5}$$

with $r_{\rm h}\approx 0.14 r_{\rm host}$ for the galaxy scale halo [16] and $\alpha\approx 1.9$ [15, 17]. The normalization $n_0$ is fixed by setting $N(>10^8\,M_\odot)\approx 100$ (see [10] and references therein). The density profile of each subhalo is also assumed to be a NFW or Moore profile. To determine the density parameters of each subhalo, we use the concentration-mass relation given in Ref. [18]. The procedure of determining the parameters is as follows. For a halo with mass $m_{\rm sub}$, the concentration is derived according to the $c_{\rm sub}-m_{\rm sub}$ relation. Then we have $r_{\rm s}^{\rm NFW}=r_{\rm sub}/c_{\rm sub}$ and $r_{\rm s}^{\rm Moore}=r_{\rm sub}/0.63c_{\rm sub}$ following the definition of concentration [18]. Finally, $\rho_{\rm s}$ is determined by the subhalo mass.

To calculate the annihilation flux of photons from the subhalo population, we define the average density square as

$$\langle\rho^2_{\rm sub}\rangle(r)=\int{\rm d}m_{\rm sub}\frac{{\rm d}n}{{\rm d}m_{\rm sub}\cdot 4\pi r^2{\rm d}r}\times\int_{V_{\rm sub}}\rho^2_{\rm sub}{\rm d}V, \tag{6}$$

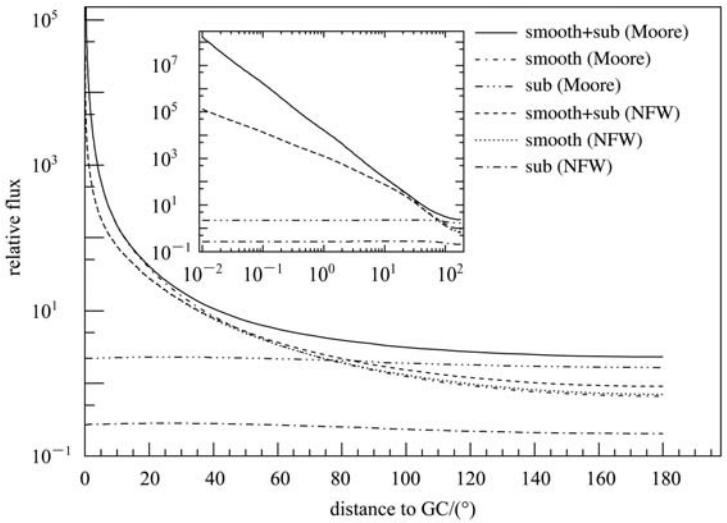


Fig. 1. The angular distribution of DM annihilation luminosity ($J$ factor) in the Milky Way. The inner plot uses a log scale for the $x$ axis to show the details in the most central region.

where $\mathrm{d}V$ integrates over the volume of the subhalo. Replacing $\rho^2$ in $J(\psi)$ in Eq. (1) with $\langle\rho^2_{\rm sub}\rangle$ we calculate the photon flux from DM annihilation in the subhalos.

The $J(\psi)$ factor as a function of the angle $\psi$ away from the GC direction is shown in Fig. 1. It can be seen that for the smooth halo, the annihilation flux is highly concentrated in the GC. The substructure contribution is nearly isotropic in all directions. At large angles away from the GC, the substructure component may dominate the annihilation flux of the Moore profile.

## 3 Detectability analysis

### 3.1 Backgrounds

We first introduce the backgrounds that are essential for the detectability analysis of the DM-induced monochromatic $\gamma$-ray signal. The backgrounds include charged CR particles, such as all kinds of nuclei, electrons and positrons, and continuous $\gamma$-rays.

The CR nuclei and electrons/positrons can be rejected through the design of a particle identification technique of the detector. However, there are still a few particles that may be misidentified as photons and form the background. The combined nuclei flux, mostly proton and Helium nuclei, can be written as [19]

$$\phi_{\rm n}(E)=1.49\,(E/{\rm GeV})^{-2.74}\,{\rm cm}^{-2}\cdot{\rm s}^{-1}\cdot{\rm sr}^{-1}\cdot{\rm GeV}^{-1}, \tag{7}$$

which is an empirical formula from the combined result of many measurements. For the electron plus positron spectrum, we adopt a broken power law parameterization

$$\phi_{\rm e}(E)=1.5\times10^{-11}\left[1+(E/900\ {\rm GeV})^{10/3}\right]^{-0.33}\times(E/900\ {\rm GeV})^{-3.0}\,{\rm cm}^{-2}\cdot{\rm s}^{-1}\cdot{\rm sr}^{-1}\cdot{\rm GeV}^{-1} \tag{8}$$

according to the recent measurements by Fermi [20] and HESS [21, 22]. In the following, we employ two efficiencies, $\eta_{\rm n}$ and $\eta_{\rm e}$, to represent the rejection power of the charged CRs.

Then we come to the continuous $\gamma$-ray backgrounds. The first $\gamma$-ray background is the all-sky diffuse $\gamma$-ray emission, including Galactic and extragalactic. For the extragalactic $\gamma$-ray background, we use the new measurement made by Fermi [23]

$$\phi_\gamma^{\rm extra}(E) = 6.57\times10^{-7}\,(E/{\rm GeV})^{-2.4}\,{\rm cm}^{-2}\cdot{\rm s}^{-1}\cdot{\rm sr}^{-1}\cdot{\rm GeV}^{-1}. \tag{9}$$

The Fermi result of extragalactic $\gamma$-ray emission is steeper than that obtained by EGRET [24], which will result in an order of magnitude lower background when extrapolating to high energies ($\sim$TeV).

Fermi Collaboration also reported some data about the Galactic diffuse $\gamma$-ray emission (e.g., [23, 25, 26]), which is consistent with the results given by EGRET except for the "GeV excess" [27]. Since the full Fermi data are unavailable at present, we use the EGRET data on the Galactic diffuse $\gamma$-ray emission in this work. The Galactic diffuse $\gamma$-ray flux is parameterized as [28]

$$\phi_\gamma^{\rm galac}(E)=N_0(l,b)\times10^{-6}\,(E/{\rm GeV})^{-2.7}\,{\rm cm}^{-2}\cdot{\rm s}^{-1}\cdot{\rm sr}^{-1}\cdot{\rm GeV}^{-1}, \tag{10}$$

where

$$N_0=\begin{cases}\dfrac{85.5}{\sqrt{1+(l/35)^2}\sqrt{1+(b/1.8)^2}}+0.5 & |l|\leqslant30^\circ\\ \dfrac{85.5}{\sqrt{1+(l/35)^2}\sqrt{1+[b/(1.1+0.022|l|)]^2}}+0.5 & |l|>30^\circ\end{cases}, \tag{11}$$

in which the galactic longitude $l$ and latitude $b$ are expressed in units of degrees. To make use of this measurement, we have to extrapolate Eq. (10) to higher energies.

Besides the diffuse $\gamma$-ray emission, there are additional sources in the GC region. Since the GC region is very important for DM searches, the $\gamma$-ray sources in the GC region require more attention. HESS observation showed that there was diffuse $\gamma$-ray emission in the region $|l|<0.8^\circ$, $|b|<0.3^\circ$ (GC ridge) on top of the diffuse background [29]. The spectrum is

$$\phi_\gamma^{\rm GC\text{-}diff}(E) = 1.28\times10^{-4}\,(E/{\rm GeV})^{-2.29}\,{\rm cm}^{-2}\cdot{\rm s}^{-1}\cdot{\rm sr}^{-1}\cdot{\rm GeV}^{-1}. \tag{12}$$

Also, there is at least one gamma-ray point source in the Galactic center area, which is labeled as 3EG J1746-2851 in the EGRET catalog [30], HESS J1745-290 in the HESS catalog [31] and 0FGL J1746.0-2900

in the Fermi catalog [32]. The energy spectrum of this source given by HESS is [33]

$$\phi_\gamma^{\rm point}(E) = 2.5\times10^{-7}\,(E/{\rm GeV})^{-2.21}\,{\rm cm}^{-2}\cdot{\rm s}^{-1}\cdot{\rm GeV}^{-1}, \quad (13)$$

which is valid between 200 GeV and 10 TeV.

The differential fluxes of all the backgrounds mentioned above are plotted in Fig. 2. Here we show the results within the circle with 1 degree radius around the GC. The electron and nuclei fluxes are multiplied by factors $10^{-3}$ and $10^{-6}$, respectively, which represent the typical rejection power of a $\gamma$-ray detector. We can see that the largest background is the diffuse source and the point source in the GC region. The Galactic diffuse $\gamma$-ray emission is also important in the GC. However, for the sky regions far away from the GC, the extragalactic background would also become important.

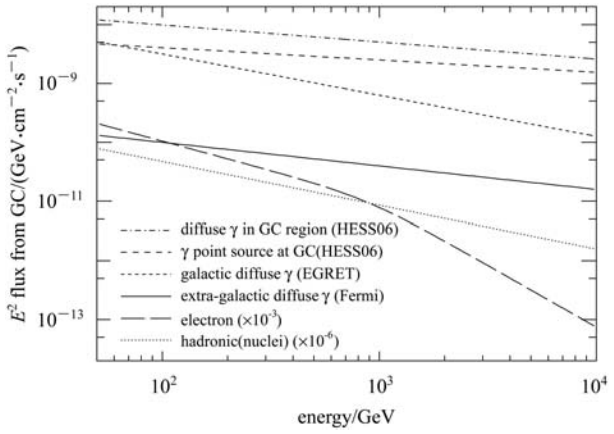


Fig. 2. Spectra of the possible backgrounds from the 1 degree region around the GC.

### 3.2 Ideal detector

The sensitivity of monochromatic $\gamma$-ray detection is determined by the performance of a detector. First, we need particle discrimination to reject most of the charged CRs, say nuclei and electrons/positrons. This can be done through charge detection, neutron detection and shower shape identification in a calorimeter. The continuous $\gamma$-rays can be suppressed by improving the detector energy resolution. Furthermore, as can be seen in Fig. 1, the small region around the GC is the best candidate for line spectrum $\gamma$-ray detection. Thus good angular resolution will also be effective in increasing the signal-to-noise ratio.

To simplify the study, we characterize the detector with some static parameters of performance, that is, the parameters don't change with incident energy, direction, or particle type, like the energy resolution, the angular resolution, the field of view, and the rejection power of electrons and nuclei. The effective area of detector and exposure time are also key factors in the detection. However, the overall performance can be easily scaled given a different effective area and exposure time. With the results of ideal detectors, we can provide the requirement of a real detector.

The default set of parameters of the ideal detector setup in this work is assumed to be effective area 1 m$^2$, energy resolution 1.5%, angular resolution 0.5°, field of view 90°, electron rejection power $10^{-4}$, and proton rejection power $10^{-7}$. This set of performances is close to a planned next generation space-borne $\gamma$-ray detector in the coming years, mounted on the Chinese space station.

### 3.3 Sensitivity calculation

The event counts on a detector can be written as

$$N_i = \eta_i\cdot T_{\rm eff}\cdot A\cdot f_i, \quad (14)$$

where $\eta_i$ is the detection efficiency of an incident particle, usually assumed to be 90% for a photon, and equal to the rejection power for electrons and nuclei, $T_{\rm eff}$ is the effective exposure time for a given source or small sky region, $A$ is the active area of the detector, and $f_i$ is the flux of signal or background in a given energy range and sky region. For a detector with energy resolution $\sigma_{\rm e}$, $f_i$ can be derived according to the differential flux $\phi$

$$f_i = \int_{\Delta\Omega}{\rm d}\Omega\int_{E_\gamma-3\sigma_{\rm E}}^{E_\gamma+3\sigma_{\rm E}}{\rm d}E\;\phi_i(E,l,b). \quad (15)$$

Here we choose the energy window to be $\pm3\sigma_{\rm E}$ around $E_\gamma$, and $\Delta\Omega$ refers to the chosen observation field. Note that for a point source the above integral with respect to $\Omega$ disappears.

The detection significance is defined as $S = N_{\rm s}/\sqrt{N_{\rm b}}$ with $N_{\rm s}$ the count of the signal and $N_{\rm b}$ the count of the background. The sensitivity can be derived as the minimal signal flux needed for detection significance $S = 5$.

## 4 GC region sensitivity with analytical estimate

In this section, we estimate the sensitivity of monochromatic $\gamma$-ray detection from the GC region by DM annihilation. We choose a typical planar calorimeter type detector with 1 m × 1 m size. With one year of flight on the orbit of the International Space Station (ISS) and the assumption of a 90 degree field of view, the effective exposure time is

$\sim 7.9\times10^6$ s, which is about 1/4 of a year. More details about the effective exposure time can be found in Fig. 6.

The background event number is

$$\begin{aligned} N_{\rm b} &= N_\gamma^{\rm galac}+N_\gamma^{\rm extra}+N_{\rm e}+N_{\rm n}+N_\gamma^{\rm point}+N_\gamma^{\rm GC\text{-}diff} \\ &= T_{\rm eff}A\int_{E_\gamma-3\sigma_{\rm E}}^{E_\gamma+3\sigma_{\rm E}}{\rm d}E \\ &\quad\times\Bigg[\int_{\Delta\Omega}{\rm d}\Omega\eta\phi_\gamma^{\rm galac}(E) \\ &\quad+\Delta\Omega\left(\eta\phi_\gamma^{\rm extra}(E)+\eta_{\rm e}\phi_{\rm e}(E)+\eta_{\rm n}\phi_{\rm n}(E)\right) \\ &\quad+\eta\phi_\gamma^{\rm point}(E)+\eta\Omega_{\rm GC\ ridge}\phi_\gamma^{\rm GC\text{-}diff}(E)\Bigg], \end{aligned} \tag{16}$$

where $\Delta\Omega=\pi(\sigma_{\rm d}+1)^2\times(\pi/180)^2$ is the solid angle considered for event direction selection, in order to keep the same number of signal events, where $\sigma_{\rm d}$ is the detector resolution angle in units of degrees. Another method of event direction selection is to keep events of 1° from GC after point spreading of the detector angle resolution. Considering that the largest backgrounds come from point-like sources from GC, and they expand the same as the cuspy Moore dark matter profile, the one-degree selection after expansion would result in the same level of decrease in both signal and background event number, which means poorer sensitivity. On the other hand, if we select events with a larger radius, we can keep basically the same number of signal events and achieve better sensitivity. Therefore the minimal monochromatic photon flux from DM annihilation within $\sim1$ degree around the GC is $f_{\rm min}=5\sqrt{N_{\rm b}}/\eta T_{\rm eff}A$, for a $5\sigma$ detection.

The results of $f_{\rm min}$ for different detector performance, i.e., different energy resolution, angular resolution, electron rejection and nuclei rejection, respectively, are shown in Fig. 3. The default detector performance settings are: energy resolution 1.5%, angular resolution 0.5°, electron rejection $10^{-4}$ and nuclei rejection $10^{-7}$. The different performances used in the calculation are summerized in Table 1. The dots and

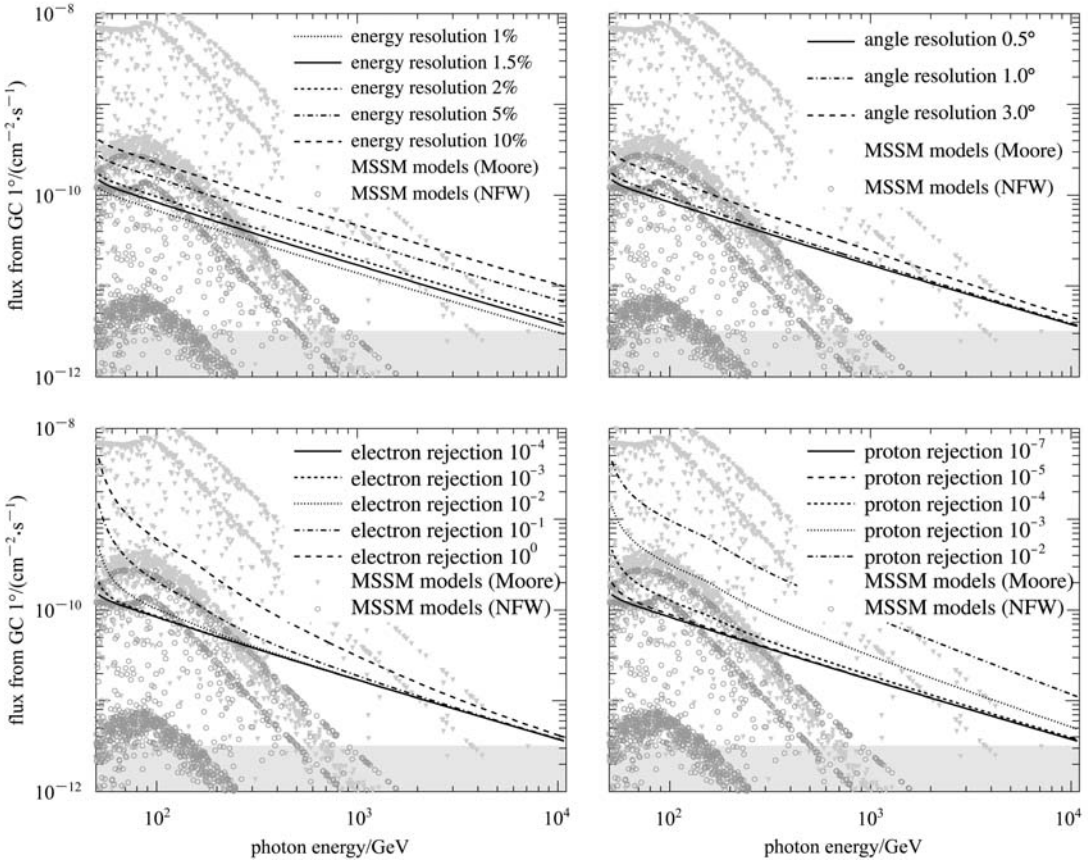


Fig. 3. The sensitivity in the Galactic center area with different detector features: energy resolution (top-left), angular resolution (top-right), electron rejection (bottom-left), nuclei rejection (bottom-right). The default settings are: energy resolution 1.5%, angular resolution 0.5°, electron rejection $10^{-4}$ and nuclei rejection $10^{-7}$. The gray area at the bottom of each panel represents the flux corresponding to less than one event per year for a 1 m$^2$ detector.

triangles in the figure are the MSSM model predictions with a random scan in the eight-dimensional parameter space as introduced in Sec. 2.1. Both Moore and NFW profiles are calculated and plotted. It is shown that the default detector configuration is powerful enough to probe much of the MSSM parameter space for the model with DM density as cuspy as the Moore type. If the DM density profile is NFW-like, the sensitivity will be worse. We will further discuss the effects of different density profiles later.

Table 1. GC detectability calculation configuration.

| | |
|---|---|
| common setup | detector area: 1 $m^2$, exposure time: $7.9\times10^6$ s, energy range: 50 GeV–10 TeV |
| energy resolution | 1%, 1.5%, 2%, 5%, 10% |
| angular resolution | 0.1°, 0.3°, 0.5°, 1.0°, 3.0° |
| electron rejection | $10^0$, $10^{-1}$, $10^{-2}$, $10^{-3}$, $10^{-4}$ |
| proton rejection | $10^{-2}$, $10^{-3}$, $10^{-4}$, $10^{-5}$, $10^{-7}$ |

In Fig. 4 we show a comparison of sensitivities for longer exposure and larger area of the same type of detector.

In Fig. 5, the minimal detectable cross section is shown for $\gamma\gamma$ (left) and $\gamma Z_0$ (right) channel, respectively. In this plot, the default detector performance is adopted, and we show the results for the NFW and Moore profiles, with different sky regions. It is shown that for the NFW profile, the detectability will be orders of magnitude worse than that for the Moore profile. The significance of the NFW profile first increases and then decreases with the angle radius of observation area centered at the GC, and reaches its maximum at the angle radius of about 10°. We also note that the choice of sky area does not affect the significance of the NFW profile significantly, compared with that for the Moore profile. It can be understood that for the Moore profile the signal flux drops very fast with the increase in the angle distance to the GC, which leads to a fast decrease in the signal-to-noise ratio. Therefore the large-angle average results in a worse sensitivity than the case focusing on the small region around the GC.

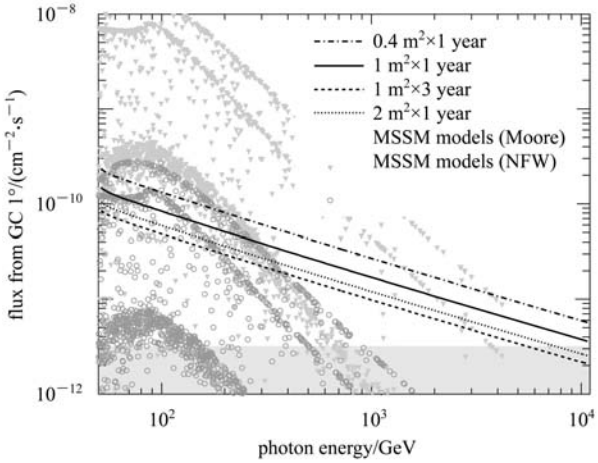


Fig. 4. The sensitivity with different exposure factors and detector areas.

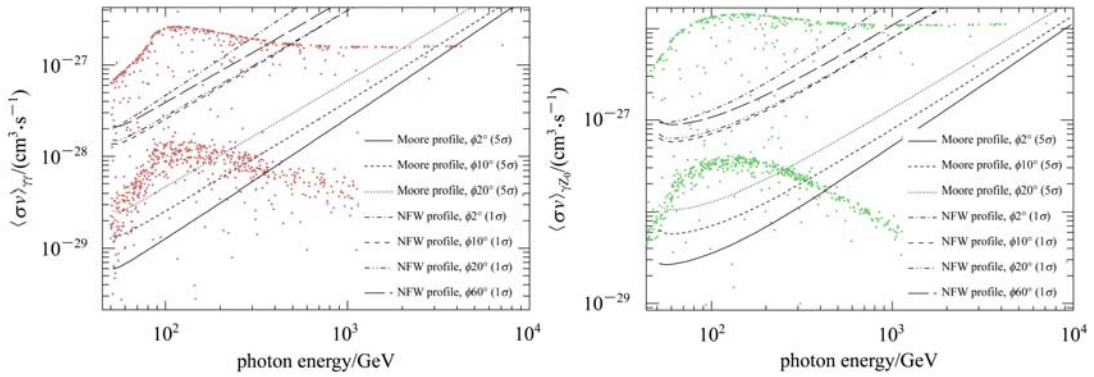


Fig. 5. The minimal detectable cross section for $\gamma\gamma$ (left) and $\gamma Z_0$ (right) channels in different observation areas.

## 5 Whole sky scan sensitivity with Monte-Carlo simulation

In this section, we discuss the all-sky observation with scan mode. The effective exposure time is non-uniform in different directions for a specific orbit of the detector. Therefore the simple analytical method discussed in the previous section no longer works. We turn to use a fast Monte-Carlo method to simulate the counts of signal and background, and calculate the sensitivity.

### 5.1 Simulation configuration

The flight orbit is assumed to be the orbit of ISS. We put an ideal detector on the orbit, and calculate

the signal and background particle counts by Monte-Carlo sampling. We take the orbit data of ISS in 2003 as an example. The orbit of ISS has not changed too much in the period of several years. The sky-map of exposure time is plotted in Fig. 6.

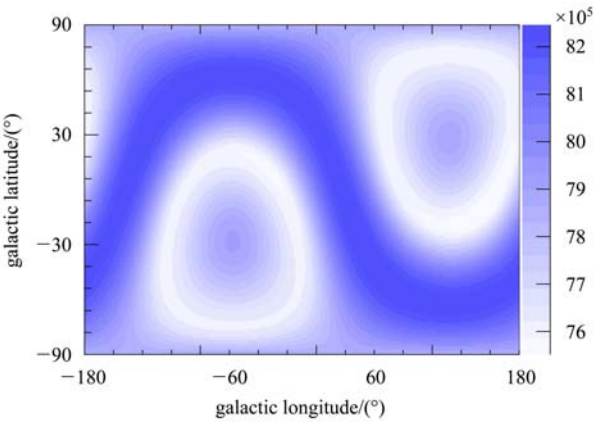


Fig. 6. Sky-map of effective exposure time according to the 2003 ISS orbit data. The whole sky area is divided into $360 \times 180$ cells, with $1^\circ \times 1^\circ$ of each cell. The effective exposure time of each cell is calculated as $\cos(\theta)$ if $\theta < \pi/2$, and zero otherwise, where $\theta$ is the angle between the direction of the ISS and the direction of the cell. Then the effective time of each cell is accumulated in an interval of one second for a period of one year ($3.15 \times 10^7$s).

We choose detectors with a series of property parameters, including energy resolution, field of view, and electron and nuclei rejection powers. Seven neutralino masses, between 50 GeV and 1200 GeV, are chosen in the simulation. The details of the configurations are listed in Table 2.

Table 2. Survey simulation configuration.

| | |
|---|---|
| common setup | detector area: $1\,\mathrm{m}^2$, flight time: 1 year, flight orbit: ISS orbit |
| simulated energy/GeV | 77.6, 199.7, 416.3, 611.4, 808.6, 1006.0, 1220.9 |
| energy resolution | 1%, 1.5%, 2%, 5% |
| field of view | 40°, 60°, 90° |
| electron rejection | $10^{-1}$, $10^{-2}$, $10^{-3}$, $10^{-4}$ |
| proton rejection | $10^{-4}$, $10^{-5}$, $10^{-6}$, $10^{-7}$ |

To get better statistics, a large enough cross section was chosen in the simulation. The photons from $\gamma\gamma$ and $\gamma Z_0$ annihilation channels are not distinguished, and only a sensitivity for single gamma line emission is given. Actually, the photons from these two channels cannot be discriminated when the neutralino mass is larger than several hundred GeV, and if the neutralino mass is small, there could be two peeks on the photon energy spectrum, thus the sensitivity would be higher.

The overall contribution from DM annihilation, not only the smooth halo but also the substructures, is taken into account. In the simulation, we use the Moore profile for both the smooth halo and the subhalos. To compare with theory predictions, the model points are plotted along with the minimum detectable curves. In the calculation, both Moore and NFW profiles are used. Also, the contribution of substructures and a smooth halo are summed.

### 5.2 Event generation and reconstruction simulation

The basic procedure of the simulation can be divided into two phases. The first is the generation of the event samples according to the angular and energy distributions of each component, including the signal and backgrounds. The second phase simulates the event reconstruction process based on the detector performances.

For the signal events, the energy of the generated photon is monochromatic for a given neutralino mass. The spatial distribution follows the result, as shown in Fig. 1. The energy spectra and angular distributions of backgrounds are described in Sec. 3.1. In the simulation, we also need to know the direction of the detector. The detector pointing direction is set to be the same as the direction of ISS.

The events are generated in intervals of one second in detector operation time. To simplify the simulation code, the static event rate for each component is used. The event rate is set to be the maximum value that can be received by the detector with acceptance $4\pi \cdot A$, for the energy range from 30 GeV to 1400 GeV, and a Poisson smear is used when the event number in the one-second interval is too small. However, the actual events received by a specific detector will be much smaller than the above value since the effective area for photons with a large incident angle will decrease. This effect is taken into account in the second phase through an efficiency factor $\eta$, defined as $\eta_i \cos(p)$ when $p < p_{\mathrm{FOV}}$, and 0 when $p \geqslant p_{\mathrm{FOV}}$, where $p$ is the angle between the incident photon and the detector pointing direction, $p_{\mathrm{FOV}}$ is the maximum receiving angle of incident particles, and $\eta_i$ is the selection efficiency for different incident particles. For photons, the selection efficiency is usually assumed to be 90%. For electrons and nuclei events, the detector rejection power is used as the selection efficiency. Then one event is kept with probability $\eta$.

The events kept in the efficiency selection are then reconstructed. The reconstruction of energy is simply implemented by a Gaussian smear of the injection photon energy. The Gaussian width is $\sigma_e$, which represents the energy resolution of the detector. The nuclei rejection and electron rejection are simulated as a fixed pass rate, as mentioned before. The passed electrons and nuclei are reconstructed in the same way as photons. Fig. 7 shows a sample reconstructed energy spectrum for the neutralino mass 416 GeV. The direction reconstruction simulation is in the same way as energy reconstruction, with a two-dimensional Gaussian smear.

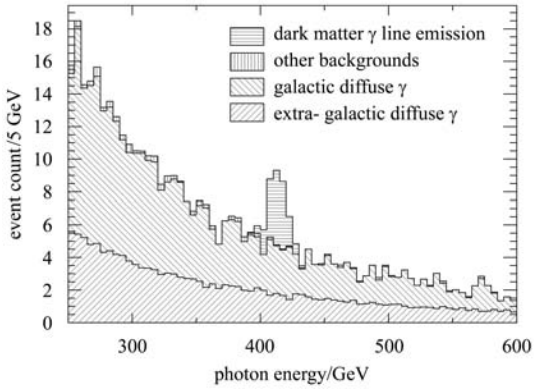


Fig. 7. A sample reconstructed stacked photon energy spectrum, for neutralino mass 416 GeV.

### 5.3 Results of simulation

The results of sensitivities for scan observation are shown in Fig. 8 for different detector performances. The area of the detector is adopted as 1 m × 1 m. The points represent the MSSM model predicted fluxes of the all-sky DM annihilation, with substructures included for both Moore and NFW profiles. Compared with the results of the GC, the scan mode will be less sensitive for detecting the DM annihilation signal by more than one order of magnitude.

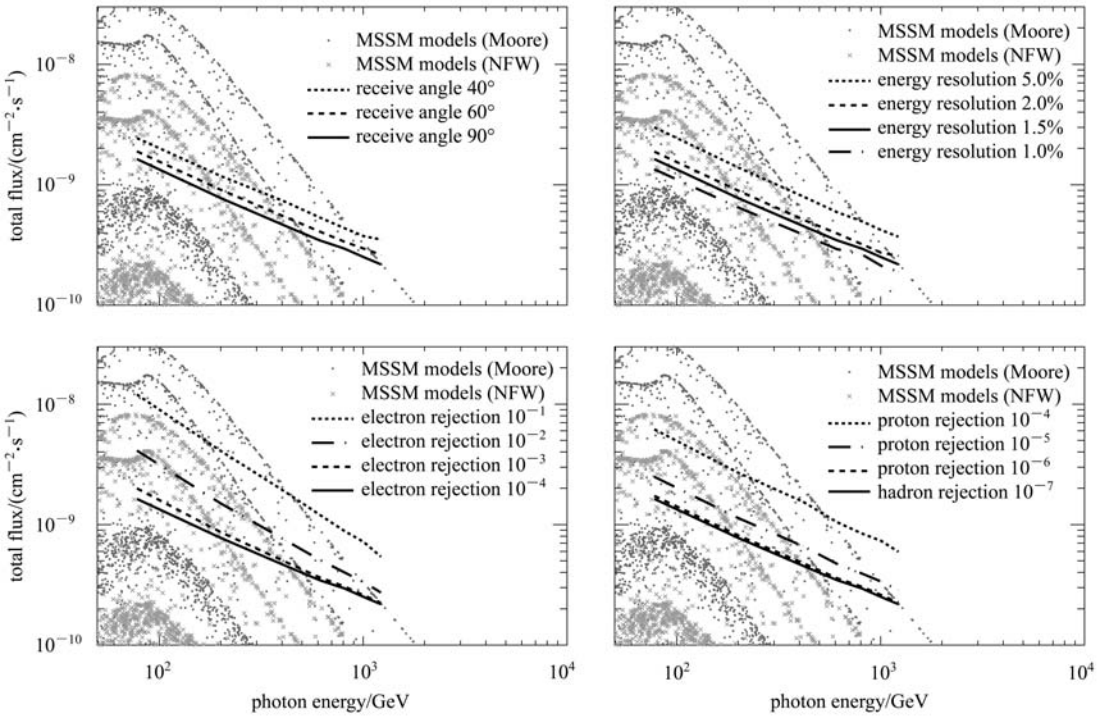


Fig. 8. The sensitivity of line emission detection for all-sky scan mode with different detector performance. Top-left: comparison among different maximum receiving angles (fields of view); top-right: comparison among different energy resolutions; bottom-left: comparison among different electron rejection powers; bottom-left: comparison among different nuclei rejection powers. The default parameters are energy resolution 1.5%, maximum receiving angle 90°, electron rejection $10^{-4}$, and proton rejection $10^{-7}$.

## 6 Discussion and conclusion

In this work, we studied the strategy and feasibility of the monochromatic γ-ray detection from DM annihilation. We studied the detectability of the monochromatic γ-rays from the GC and from the dark matter halo and subhalos, by analysis and numerical Monte-Carlo simulation. The detector performance is studied for the purpose of monochromatic γ-ray detection.

The sensitivity depends on the observation region and the DM density profiles. According to the Moore profile, the sensitivity of the GC region would be much higher than of other regions. However, this is not true for the NFW-like profiles. As we currently have little knowledge of the actual distribution, we cannot rely on a particular model. Until now, high energy gamma observations, such as the HESS and Fermi ones, have not seen any evidence in the GC region. A safe strategy could start from the scan mode, then focus on the interesting area if any evidence is found. On the other hand, the GC is always an interesting region for possible DM signals. The observation of the GC should be tuned as much as possible.

In order to detect the monochromatic $\gamma$-ray emission of DM annihilation in scan mode, the energy resolution and geometry factor, both the detector area and the field of view are the most important detector features. However, The resources are usually very limited on orbit, on both detector mass and power supply. With a given mass of the detector, a thinner calorimeter would lead to a larger active area. On the other hand, thinner calorimeters usually have poorer energy resolution. Therefore, to get better sensitivity, a careful balance is needed in detector design. Also, it is preferable for any detector design that would limit the field of view of the detector to be avoided. At low energies ($< 300$GeV), the ability to reject cosmic-ray background, both electrons and nuclei, is also important. To keep the cosmic-ray background low enough, that is, lower than the major background, diffuse $\gamma$, at least $10^{-3}$ electron rejection and $10^{-6}$ proton rejection, are required.

If we are focusing on GC or another interesting region in pointing mode, the angular resolution, instead of the field of view, will become very important. In the GC region, the $\gamma$-ray emission is complex: several point sources exist there. Thus good angular resolution is needed to separate them, and to suppress these point source backgrounds. Of course, the energy resolution and detector area are still important features in order to detect monochromatic $\gamma$-rays. Also, at low energy, the rejection power requirements of electrons and protons are the same as in the scan mode.

## References


1 Gondolo P, Edsjö J, Ullio P et al. Journal of Cosmology and Astro Particle Physics, 2004, **7**: 8
2 Catena R, Ullio P. Journal of Cosmology and Astroparticle Physics,2010, **8**: 4
3 Salucci P, Nesti F, Gentile G, Frigerio Martins C. Astron. Astrophys., 2010, **523**: A83+
4 Komatsu E, Smith K M, Dunkley, J et al. ArXiv e-prints, 2010, arXiv:1001.4538
5 Navarro J F, Frenk C S, White S D M. Astrophys. J, 1997, **490**: 493
6 Moore B, Quinn T, Governato F, Stadel J, Lake G. Mon. Not. Roy. Astron. Soc., 1999, **310**: 1147
7 Navarro J F, Ludlow A, Springel V et al. Mon. Not. Roy. Astron. Soc., 2010, **402**: 21
8 Jing Y P, Suto Y. Astrophys. J. Lett., 2000, **529**: L69
9 Berezinsky V S, Gurevich A V, Zybin K P. Physics Letters B, 1992, **294**: 221
10 Lavalle J, YUAN Q, Maurin D, BI X. Astron. Astrophys., 2008, **479**: 427
11 Tormen G, Diaferio A, Syer D. Mon. Not. Roy. Astron. Soc., 1998, **299**: 728
12 Moore B, Ghigna S, Governato F et al. Astrophys. J. Lett., 1999, **524**: L19
13 Ghigna S, Moore B, Governato F et al. Astrophys. J, 2000, **544**: 616
14 Zentner A R, Bullock J S. Astrophys. J, 2003, **598**: 49
15 GAO L, White S D M, Jenkins A, Stoehr F, Springel V. Mon. Not. Roy. Astron. Soc., 2004, **355**: 819
16 Diemand J, Moore B, Stadel J. Mon. Not. Roy. Astron. Soc., 2004, **352**: 535
17 Springel V, WANG J, Vogelsberger M et al. Mon. Not. Roy. Astron. Soc., 2008, **391**: 1685
18 Bullock J S, Kolatt T S, Sigad Y et al. Mon. Not. Roy. Astron. Soc., 2001, **321**: 559
19 Gaisser T K, Honda M, Lipari P, Stanev T. International Cosmic Ray Conference, 2001, **5**: 1643–+
20 Abdo A A, Ackermann M, Ajello M et al. Physical Review Letters, 2009, **102**: 181101
21 Aharonian F, Akhperjanian A G, Barres de Almeida U et al. Physical Review Letters, 2008, **101**: 261104
22 Aharonian F, Akhperjanian A G, Anton G et al. Astron. Astrophys., 2009, **508**: 561
23 Abdo A A, Ackermann M, Ajello M et al. Physical Review Letters, 2010, **104**: 101101
24 Sreekumar P, Bertsch D L, Dingus B L et al. Astrophys. J, 1998, **494**: 523
25 Abdo A A, Ackermann M, Ajello M et al. Astrophys. J, 2009, **703**: 1249
26 Abdo A A, Ackermann M, Ajello M et al. Physical Review Letters, 2009, **103**: 251101
27 Hunter S D, Bertsch D L, Catelli J R et al. Astrophys. J, 1997, **481**: 205
28 Bergström L, Ullio P, Buckley J H. Astroparticle Physics, 1998, **9**: 137
29 Aharonian F, Akhperjanian A G, Bazer-Bachi A R et al. Nature, 2006, **439**: 695
30 Mayer-Hasselwander H A, Bertsch D L, Dingus B L et al. Astron. Astrophys., 1998, **335**: 161
31 Aharonian F, Akhperjanian A G, Bazer-Bachi A R et al. Physical Review Letters, 2006, **97**: 221102
32 Abdo A A, Ackermann M, Ajello M et al. Astrophys. J. Supp., 2009, **183**: 46
33 Aharonian F, Akhperjanian A G, Anton G et al. Astron. Astrophys., 2009, **503**: 817